

## Thermal infrared observations of near-Earth asteroids and data reduction<sup>7,8</sup>

### 3.1 Foreword

A major development within this study is the discussion of the results from observing programs with the 10m - Keck 1 telescope on Mauna Kea, Hawaii (Delbo et al. 2003) and with the ESO 3.6 m telescope on La Silla, Chile. Further observations have been collected with the 3.0 m NASA-Infrared Telescope Facility (IRTF) in Hawaii. In this chapter we describe the instruments, the observations and the data reduction techniques used to obtain the thermal infrared fluxes - listed in appendix A - of the target asteroids.

### 3.2 Introduction

An extended dataset of new thermal infrared observations of NEOs have been obtained in the years 2000-2003 within the framework of this Ph.D. project. A major development within this study is the discussion of the results obtained from observations carried out at the Keck-1 telescope, Mauna Kea Hawaii<sup>9</sup> on 7 nights between March 2000 and February 2002. At the Keck-1, the Long Wavelength Spectrograph (LWS) was used in imaging mode. This is a liquid helium cooled instrument for almost diffraction limited imaging and spectroscopy in the 5-20  $\mu\text{m}$  regions. Details of the instrument are given by Jones and Puetter (1993) and can be found on the Keck Observatory web site (<http://www2.keck.hawaii.edu/realpublic/inst/>). Narrow-band filters centered on 4.8, 8.0, 8.9, 10.7, 11.7, 12.5, 17.6, 17.9 and 20.0  $\mu\text{m}$  were selected for observations with this instrument. Results of the Keck observing campaigns are discussed by Delbò et al. (2003).

Several additional observations have been collected using the ESO 3.6m telescope at the European Southern Observatory in La Silla, Chile<sup>10</sup> on 10 nights between April 2001 and June 2003. The Thermal Infrared Multi-Mode Instrument (TIMMI2) was used at the ESO 3.6m telescope (see Reimann et al.,

---

<sup>7</sup> Part of this chapter is devoted to the description of the observations and the data reduction of our program with the Keck 1 telescope. Most of the radiometric diameters and albedos derived from this project have been already published by Delbo et al. (2003). Note that Table 3-1 contains three more NEAs, with respect to the equivalent table of Delbò et al. See section 3.11 for further details.

<sup>8</sup> Partially based on observation obtained at the European Southern Observatory, La Silla. Project IDs 67.C-0543, 68.C-0447, 69.C-0619, 70.C-0608, 71.C-0241

<sup>9</sup> Observations were carried out by M. Delbò, R. P. Binzel, (P.I.) and A. W. Harris.

<sup>10</sup> M. Delbò (P.I.) was the observer at the 3.6m telescope.

2000 and/or visit the ESO web page <http://www.lis.eso.org/lasilla/sciops/timmi/>). The largest majority of observations were carried out in imaging mode as well. However, the NEA 5587, observed in April 2001, was bright enough to allow TIMMI2 to be used in spectroscopic mode and reliable measurements in the 7-13  $\mu\text{m}$  range to be obtained.

At ESO, to derive accurate H magnitudes of the observed asteroids and to measure their visible lightcurves simultaneously to the thermal observations, V band CCD data were obtained simultaneously with the thermal infrared observations using the Danish Faint Object Spectrograph and Camera (DFOSC) installed at the 1.5m Danish telescope at La Silla observatory<sup>11</sup>. DFOSC, a focal reducer type spectrograph/camera, was operated in imaging mode. Details of the instrument and the telescope can be found on the ESO web page: <http://www.lis.eso.org/lasilla/Telescopes/2p2T/D1p5M/>. During the last two runs, in November 2002 and in June 2003, the 1.5 m Danish telescope was no longer offered to the ESO community. We resorted to the use of the Wide Field Imager (WFI) installed at the 2.2m ESO/MPI telescope (<http://www.lis.eso.org/lasilla/sciops/wfi/>).

The NASA-Infrared Telescope Facility (IRTF)<sup>12</sup> has also been used with the aim of performing detailed studies of selected targets. We include in this work data obtained for the NEAs 33342 (1998 WT<sub>24</sub>), 1580 Betulia, 5381 Sekmeth, 6849 Golevka and for the potentially hazardous asteroid (PHA) 35396 (1997 XF<sub>11</sub>). At the NASA-IRTF the Mid-Infrared Large-Well Imager (MIRLIN) array (Ressler et al., 1994) was used to carry out the largest majority of the observation. Details of this instrument are available on the web at (<http://cougar.jpl.nasa.gov/mirlin.html>). The NEA 35386 (1997 XF<sub>11</sub>) was studied using the Mid-Infrared Spectrometer and Imager (MIRSI) which is a collaborative visiting instrument at the NASA-IRTF (visit the web page <http://cfa-www.harvard.edu/mirsi/> and/or see Deutsch, 2003 for further details of this instrument).

In what follows, we describe the techniques that were adopted to carry out the observations, describing the ways of obtaining reliable absolute calibrated mid-IR fluxes from the ground. We discuss the data reduction process with details of the methods adopted, in particular for what concern the estimation of photometric uncertainties.

Color correction factors have to be taken into account into multi-filter photometry if the spectral energy distribution of the unknown source is very different with respect to that of the standard stars used as calibrators. These factors were calculated for the IR filters that we have used at each instrument.

---

<sup>11</sup> Visible band observations were carried by M. Di Martino and, on April 2001 run, T. Vannini's collaboration was very much appreciated.

<sup>12</sup> S.J. Bus carried out the observation. M. Delbò, A.W. Harris (P.I.), and M. Mueller carried out the data reduction and analysis.

Reduction, wavelength and absolute flux calibration are discussed for spectroscopy at TIMMI2. In section 3.10, V-band CCD observations obtained at ESO are discussed along with the data reduction process, absolute magnitude calibration and methods to derive lightcurves of fast moving objects and their H values. A final section is devoted to show observational circumstances and relevant physical characteristics for the target asteroids of the data sets on which this work is based.

### 3.3 Thermal infrared ground based observations

Due to atmospheric absorption, infrared observations from the ground are limited to a number of windows in the range 5 - 20  $\mu\text{m}$  as shown in Fig. 3.1.

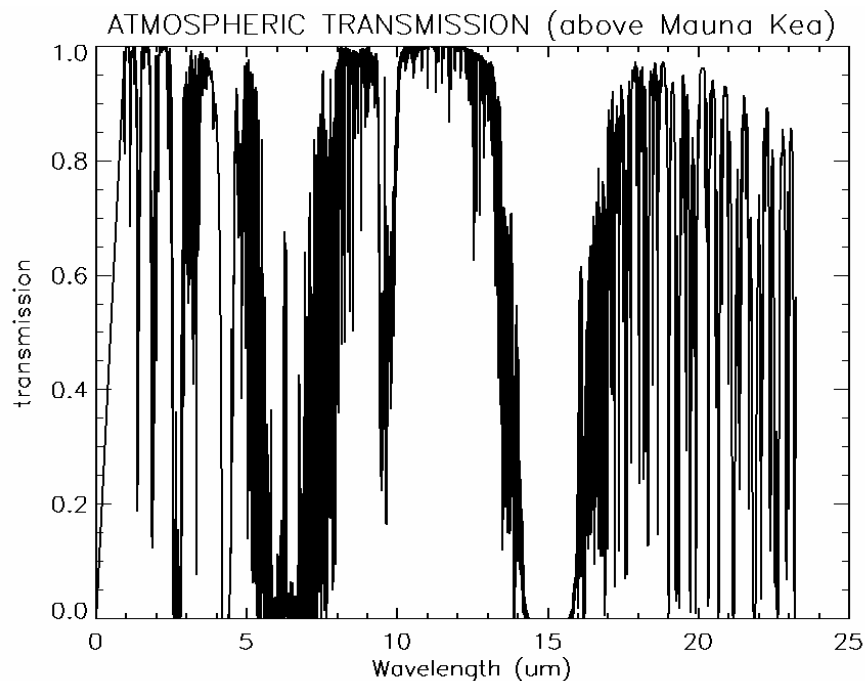


Fig. 3.1 Atmospheric transmission above Mauna Kea, Hawaii. Note the narrow window at  $5\mu\text{m}$  (M band), the ozone absorption band at about  $9.5\mu\text{m}$  in the middle of the N band. The atmosphere is opaque between  $13.5$  and about  $17\mu\text{m}$ . Beyond  $17\mu\text{m}$  up to about  $20\text{-}23\mu\text{m}$  the Q band opens.

Moreover, ground-based observations in this region are much different than the one in the optical or near infrared because of the very large thermal background flux that peaks near  $10\mu\text{m}$ . Even on infrared-optimized telescopes, the background is large compared to the flux from the brightest astronomical sources. Therefore, "chopping" and "nodding" techniques are needed to subtract the background to high precision. The accuracy to which the flux of an astronomical source can be obtained is basically limited by the background noise and by the " $1/f$ " noise due to variations in the background

caused by temperature drifts and thin clouds.  $1/f$  sky noise is suppressed with a technique called "chopping," in which the telescope's secondary mirror is oscillated in a square-wave pattern at a frequency of several Hz. The detector alternately views two fields or "beams" on the sky: A and B beams. Computing  $(A - B)$  cancels most, but not all, of the sky emission. Warm optics generates a background pattern that does not cancel out in the A-B difference. Therefore the telescope is nodded 2 – 4 times a minute to move the source from the A to the B position. By computing  $A-B - (A'-B')$  the background is properly removed.

In Fig. 3.2 the field is "chopped" with 10" amplitude northwards and nodding is performed by moving the telescope 10" westwards.

Some observations, as in the case of those obtained with the LWS at Keck, are performed by chopping the field 10" North and nodding the telescope in the opposite direction. This way of observing is sometimes called "beam-switching". If the field of view of the instrument is smaller than the chopping throw, as in the case of the LWS, only one channel is imaged on the detector at a time and half of the signal is lost when beam-switching is performed. Beam-switching is also the default observing mode for spectroscopy with the TIMMI2 at ESO. Fig. 3.3 obtained from the TIMMI2 web site ([http://www.la.eso.org/lasilla/Telescopes/360cat/timmi/images/quick\\_chop\\_nod.gif](http://www.la.eso.org/lasilla/Telescopes/360cat/timmi/images/quick_chop_nod.gif)) gives a graphical representation of the two chopping-nodding observing modes described above.

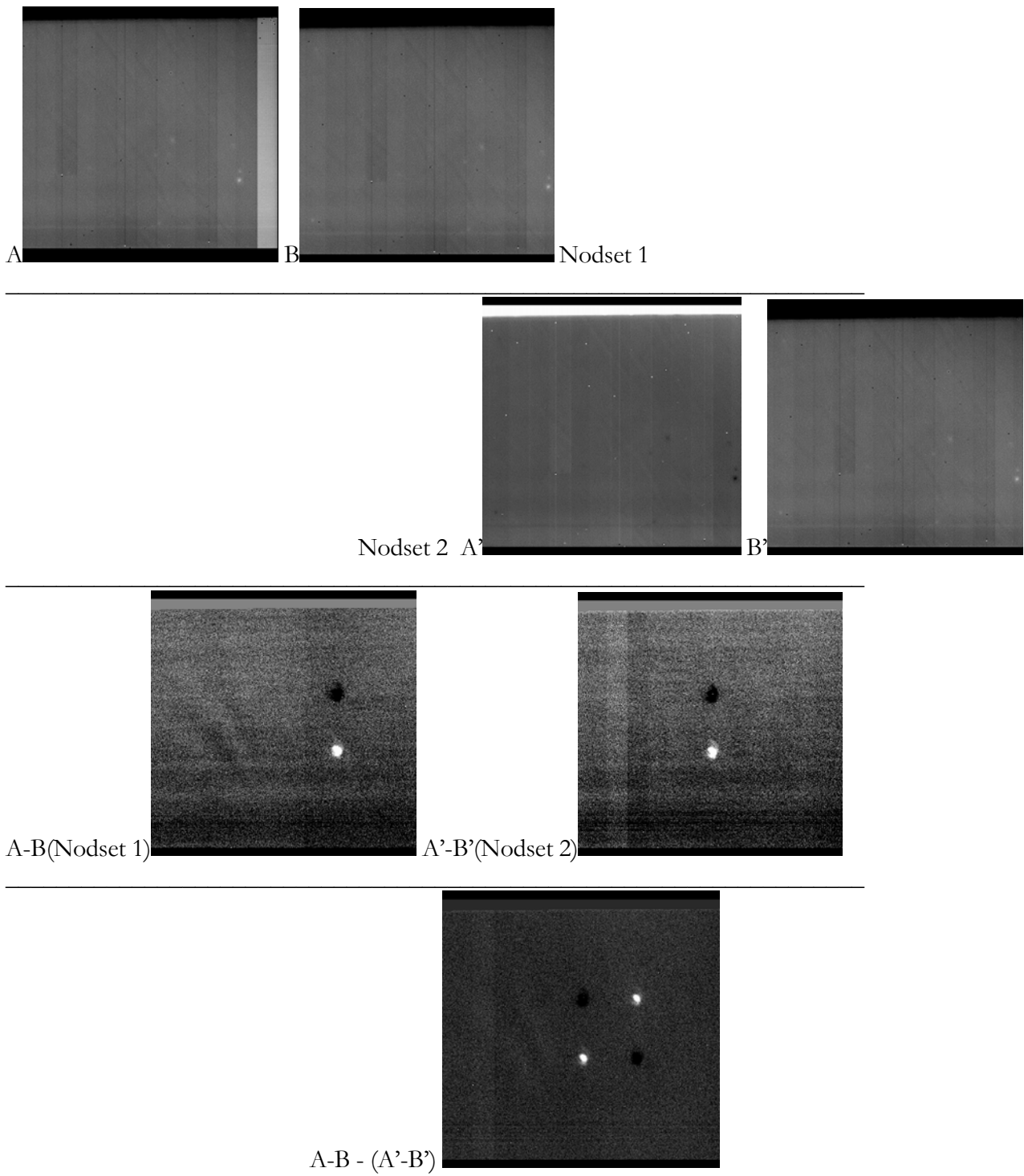


Fig. 3.2 A typical “chop-nod” observing sequence of a standard star obtained with the Thermal Infrared Multimode Instrument (TIMMI2) installed at the ESO 3.6m telescope at La Silla, Chile. Although the star is very bright, its signal is completely buried in the background radiation. Only in the differential frames it becomes visible.

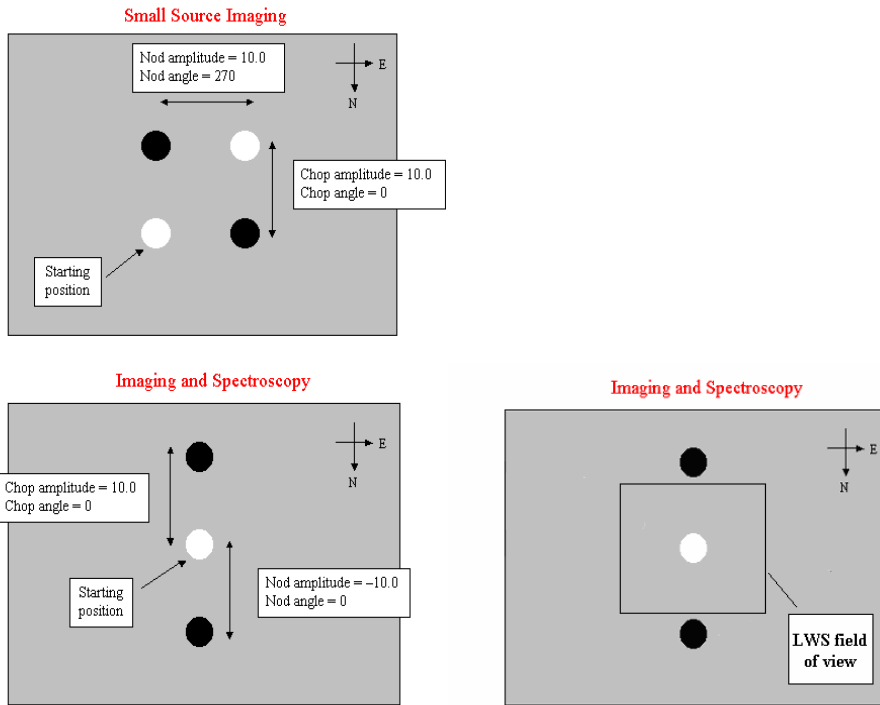


Fig. 3.3 On the left, chopping and nodding throws at TIMMI2, MIRSI and MIRLIN for small source imaging and for spectroscopy. On the right chopping and nodding at the LWS at Keck. Note that the detector field of view is too small to contain both positive and negative beams. This figure was adapted from the TIMMI2 web site: ([http://www.ls.eso.org/lasilla/Telescopes/360cat/timmi/images/quick\\_chop\\_nod.gif](http://www.ls.eso.org/lasilla/Telescopes/360cat/timmi/images/quick_chop_nod.gif))

### 3.4 Thermal IR photometry

The flux (monochromatic flux density) of an astronomical source, in the medium infrared, is measured in terms of  $W/m^2/\mu m$ . An equivalent unit is the Jansky (Jy). 1 Jy correspond to  $10^{-26} W/m^2/Hz$ . Eq (3-1) allows converting fluxes from the unit of  $W/m^2/\mu m$  to Janskys.

$$F_{Jy}(\lambda) = F_{W/m^2/\mu m}(\lambda) \times \lambda^2 \times 0.33357 \times 10^{12} \quad (3-1)$$

Infrared magnitudes are also used. A conversion table of magnitudes to Janskys and fluxes in terms of  $W/m^2/\mu m$  for a number of wavelengths can be found at the UKIRT web site: (<http://www.jach.hawaii.edu/JACpublic/UKIRT/astronomy/conver.html>).

To obtain the absolute flux of an astronomical source like the asteroids observed in this program, bright infrared standard stars are used to calculate the instrument sensitivity i.e. the photometric zero

points for each filter (i.e. how many raw counts correspond to 1 Jy in the given integration time). Given the flux of the standard at the filter effective wavelength  $F_{\text{standard}}(\lambda)$  and the instrument response raw counts in the unit time  $S''_{\text{standard}}(\lambda)$ , the instrument sensitivity  $g$  is the ratio  $F/S''$  in units of Janskys/(counts/second)<sup>13</sup>.

Eq (3-2) is used to derive the unknown magnitude of a source at a given wavelength when its signal,  $S''$ , in term of raw counts in the unit time, has been measured.  $Zp$  is the instrumental zero point magnitude,  $\chi$  the extinction coefficient and  $a$  the airmass.

$$M = -2.5 \log(S'') + Zp + \chi a \quad (3-2)$$

If  $M$  is known (for example  $M=0$  for  $\alpha$  Lyrae) and  $S''$  was measured at different airmasses, it is possible to solve for  $Zp$  and  $\chi$  by a linear least square method. The equivalent of Eq (3-2) in terms of infrared flux is:

$$F = S'' \times 10^{Zp/-2.5} \times 10^{\chi a/-2.5} \quad (3-3)$$

The second term on the right-hand side of Eq. (3-3) is the instrument (instrument + telescope + atmosphere) sensitivity. If observations of the source and the calibration standard(s) are carried out at nearly the same airmass the extinction term can be neglected and the equation reduces to:

$$F = S'' \times g \quad (3-4)$$

where  $g = 10^{-Zp/2.5}$ .

The accuracy of the final flux depends on the signal-to-noise ratio of the photometric measurement and the accuracy of our estimate of the instrument sensitivity. On the basis of Eq (3-4), we can write that:

$$\left( \frac{\sigma_F}{F} \right)^2 = \left( \frac{\sigma_{S''}}{S''} \right)^2 + \left( \frac{\sigma_g}{g} \right)^2 \quad (3-5)$$

The first term on the right-hand side of the Eq (3-5) is the inverse square of the signal-to-noise ratio of the photometric measurement. Paragraph 3.5 describes the way  $S''$  and its error can be estimated. Although an error on the value of  $g$  might arise from the finite signal-to-noise ratio of the measurements of the standard stars and the finite accuracy to which we know their absolute calibrated

---

<sup>13</sup> Double-primed letters are used to indicate quantities in terms of counts or ADUs. Primed letters indicate number of electrons while simple letters number of photons. Unprimed letters may be used for fluxes as well: i.e number of photons/s or Jy or W/m<sup>2</sup>/μm or magnitudes.

fluxes, larger fluctuations of  $g$  are caused by sky variations in emissivity and absorption during the night<sup>14</sup>. An estimate for  $\sigma_g$  might be derived from those fluctuations, if several measurements of the calibration standard(s) are available. For this reason, rather than observing standards at different airmasses and derive the extinction coefficient, it is common practice to choose a calibration star to be close in the sky to the target and observe both the object and the standard at similar airmass and close in time as much as possible.

At the Keck we have selected calibration standards taken from the database of Cohen et al. (1999). Absolutely calibrated infrared spectra for each star can be obtained directly from the web via the electronic version of the paper (see table 4) which can be found at <http://www.journals.uchicago.edu/AJ/journal/issues/v117n4/980440/980440.html>

At ESO, standards were selected directly from the TIMMI2 calibration measurements web page, (<http://www.lis.eso.org/lasilla/Telescopes/360cat/timmi/html/stand.html>). Absolute photometry of those stars for wavelength corresponding to TIMMI2 filters is given. Values for HD29291, HD124897 and HD187642 are taken from spectral energy distribution models by P. Hammersely. All other values are taken from models by Cohen et al. (1999). One-sigma flux error bars are 3%.

### 3.5 Aperture photometry and photometric uncertainties

According to the notation introduced above, let's call  $C''(x,y)$  the number of counts associated with a pixel at row  $x$  and column  $y$ . If a signal  $S''(x,y)$  is imaged on the detector we can write that  $C''(x,y) = S''(x,y) + B''(x,y)$  where  $B''(x,y)$  represents the background contribution. Aperture photometry resembles the technique used with mono-channel detectors where an aperture (a diaphragm) was used to sample the signal from the source + background and then the telescope was offsetted to a nearby patch of blank sky to sample the background. With area-array detectors a synthetic aperture is used instead and the signal is extracted by means of the following equation:

$$S'' = C''_{aperture} - A_{aperture} \times \tilde{B}'' \quad (3-6)$$

where  $C''_{aperture} = \iint_{aperture} C''(x,y) dx dy$ ,  $A_{aperture}$  is the number (often fractional) of pixels contained within the aperture and  $\tilde{B}''$  is some estimation of the background value. One of the standard methods for background estimation is to take an annulus surrounding the source, look at the pixel values within this

---

<sup>14</sup> Observations of standard stars yield usually high S/N (>50-100) photometric measurements.

region and use some algorithm to determine the value to be assigned to the background. The final result of the procedure is the signal of the source in number of counts in the unit time.

The signal-to-noise ratio determines the uncertainty to which we know the signal  $S''$ . It may be estimated experimentally using the following equation, hereafter written in unit counts:

$$\frac{S''}{N''} = \frac{S''}{\sqrt{S''/G + A_{aperture} \sigma_{B''}^2}} \quad (3-7)$$

where  $\sigma_{B''}$  is the standard deviation of the distribution of the pixel counts of the background: i.e. within the sky annulus.  $\sigma_{B''}$  is a measure of the uncertainty to which we know the value of each pixel of the background. The denominator of Eq (3-7) involves some further considerations: The first source of error is due to the Poissionian nature of the photon detection process and the second source is introduced by the background subtraction. These two error contributions are mutually independent and they have do be quadratically summed. The uncertainty associated with the signal  $S''$  is:  $\sigma_{S''}^2 = S''/G$ . This equation deserves some more comments. The number of electrons  $S'$  is  $G$  times the number of counts  $S''$ . (i.e.  $S' = G \times S''$ ). The uncertainty on the number of recoreded electrons is given by the Poisson statistic:  $\sigma_{S'} = \sqrt{S'}$ . From the error propagation formula it follows that:

$$\sigma_{S''} = \frac{\partial S''}{\partial S'} = \frac{1}{G} \sigma_{S'} = \frac{\sqrt{GS''}}{G} = \sqrt{\frac{S''}{G}}. \quad (3-8)$$

Medium infrared observations from the ground are always carried out in background-limited regime, i.e. the background is orders of magnitude larger than the signal itself, and the  $N''$  term can be estimated by the RMS value of the background in the sky annulus surrounding the source. In the signal-to-noise ratio Eq (3-7) the term due to the discrete photon detection statistic is negligible and that equation can be simplified to

$$\frac{S''}{N''} \approx \frac{S''}{\sigma_{B''} \times \sqrt{A_{aperture}}}. \quad (3-9)$$

### 3.6 Data reduction of thermal IR data

The data reduction has been performed using a modified version of the ATV package written in IDL by Aaron Barth (<http://www.astro.caltech.edu/~barth/atv/>) (Fig. 3.4). IDL, the Interactive Data Language, is developed by Research Systems Inc. (<http://www.rsinc.com/>).

The aperture photometry technique was adopted and applied to the final coadded frames to derive the source signals. No flat fielding was performed. Gain variations on the detector array were accounted for by imaging all sources on the same position (the center) of the array as far as possible. In the case of TIMMI2, MIRSI and MIRLIN images, where all four “chopped-nodded” channels were imaged on the detector, aperture photometry was applied to each channel separately. The resulting final signal was constructed by taking the sum of the raw counts of the four channels. However, in the case of faint objects, coadding the four channels and applying aperture photometry on the resulting source with higher S/N was found to provide more accurate results. This technique could not be exploited in the case of LWS/Keck observations, since only two superimposed channels were imaged on the array. To select the most appropriate photometric aperture the radial profile of the point spread function and the photometric growth-curve (the flux of the source as a function of the aperture radius) was studied for each source. Photometric growth-curves are extensively discussed by Howell (1989).

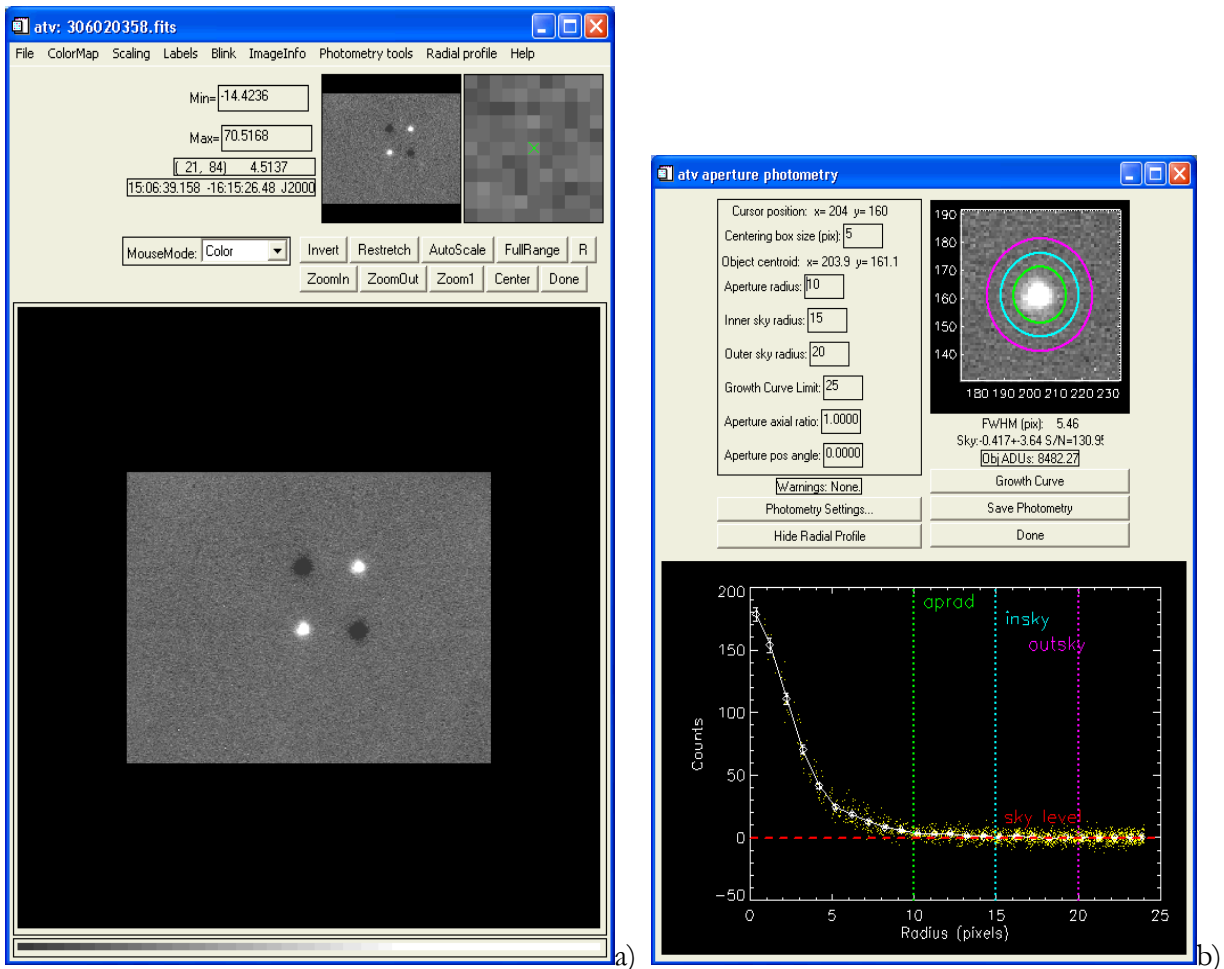


Fig. 3.4 The ATV tool: on the left (a), ATV shows a mid-IR image of a standard star obtained with the TIMMI2 at the ESO 3.6 m telescope. On the right (b), the ATV aperture photometry plug-in used to analyze one of the four chop-nod channels.

Not unexpectedly, background subtraction was found to be critical in the case of low S/N sources. The standard method for background estimation has been to take an annulus around the source, look at the pixel values within this area and use some algorithm to determine the value to be assigned to the background. This value is then multiplied by the area in pixel of the photometric aperture and subtracted from the total counts within the source area to yield a measure of the collected flux. This procedure assumes that the value for the background within the annulus is representative of its value beneath the source as well. In several thermal IR coadded observations when faint sources are imaged, however, structure in the background can be as large as the signal itself leading to a possible wrong estimate of the source flux. The study of the growth curve can yield to a much accurate estimation of the background in these cases: if the background value is correct, the flux of the source is not expected to increase by integrating within larger radii. In fact, when the photometric aperture becomes larger than the source PSF no signal is expected to be included any more and a plot of the growth curve shows a flat plateau beyond a certain aperture radius. However, this is not the case if one does the background subtraction incorrectly. For instance, if a value larger than the actual background is subtracted over increasingly larger areas, the net flux of the source decreases (see Fig. 3.5).

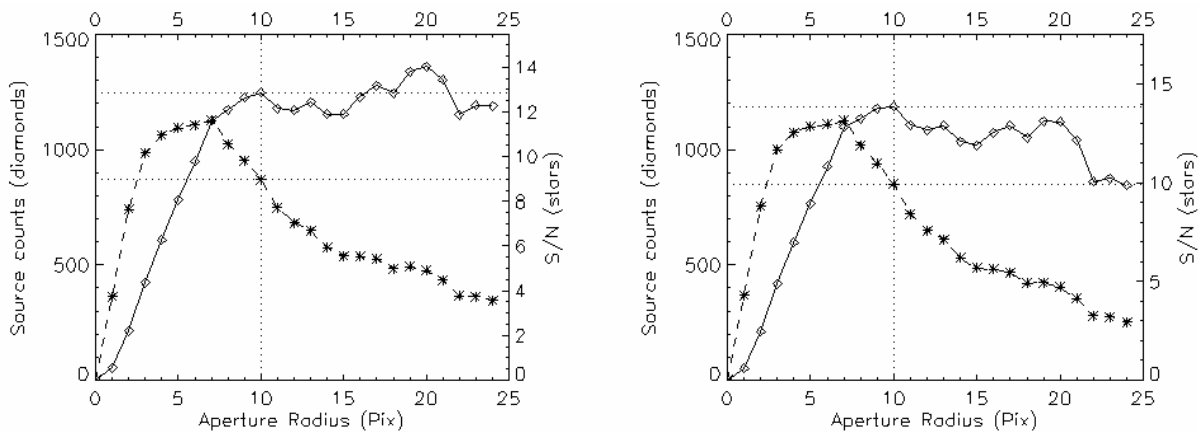


Fig. 3.5 Growth curves calculated for the one of the four chop-nod channels of a  $11.7\mu\text{m}$ -image of the asteroid 2001 LF, observed on June 03, 2003 with TIMMI2 at the ESO 3.6 m telescope (image file name: 306030840.fits). On the left plot a background value of 0.497 counts yielded 1190 counts for the source in an aperture of 10 pixels of radius. On the right, a larger background value – i.e.0.687 counts – subtracted over an increasing aperture radius causes the net flux of the source to decrease. Such background value yielded 844 counts for the source in an aperture of 10 pixel of radius.

For each source, we have selected the optimum background value by accurate adjusting the background level to make the growth curve flat at large aperture radii.

To derive the final monochromatic flux density of the target asteroids the following formula has been used:

$$F_{target}(\lambda) = F_{standard}(\lambda) \times \frac{T_{standard}}{T_{target}} \times \frac{S''_{target}}{S''_{standard}} \quad (3-10)$$

where  $F_{target}(\lambda)$  is the unknown flux of the target,  $F_{standard}(\lambda)$  is the absolute flux of the standard star within the filter band centered at  $\lambda$ ,  $S''$ 's are the background subtracted signal, in counts, measured within the photometric aperture. Eq (3-10) can be written in terms of the instrument sensitivity.

$$F_{target}(\lambda) = \frac{S''_{target}}{T_{target}} \times g(\lambda) \quad (3-11)$$

where  $g(\lambda)$  is the instrument sensitivity in Jy/(counts/second).

### 3.7 Thermal infrared observations of NEAs: a method for accurate nod-set registering

The telescopes were tracked at the differential rate predicted from the ephemerides of each target. Nevertheless, some of the final co-added images suffered a smearing effect due to track errors or the non perfect repositioning of the telescope after each nod was performed.

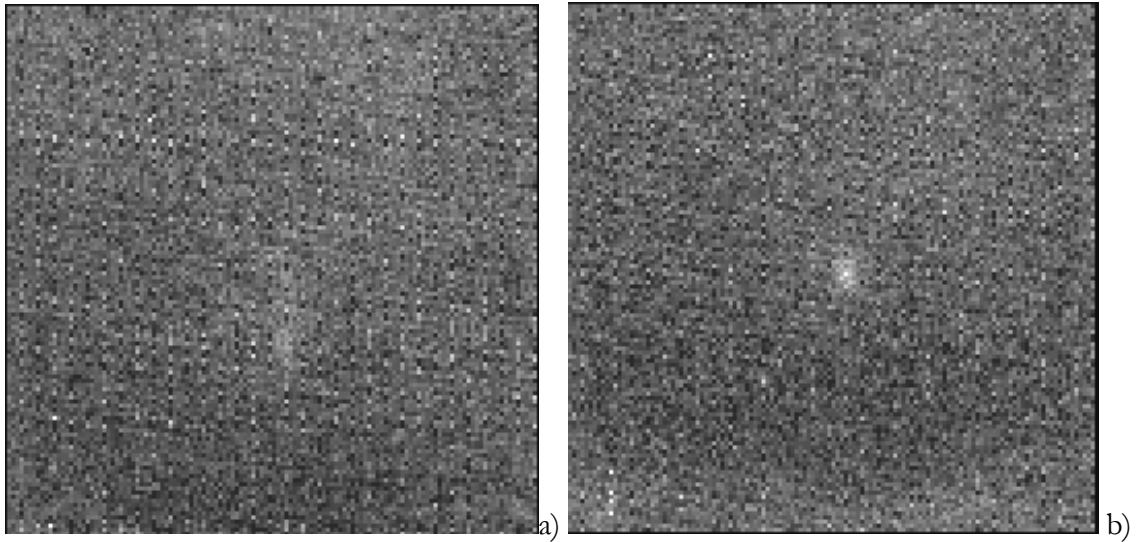


Fig. 3.6 On the right (a), strong smearing effect in the coadded LWS image of the asteroid 2002 CT<sub>46</sub> without registering. (b) the same dataset but registering of each nodeset before coadding was performed. The improvement in the S/N is clearly evident. Further, the registered PSF more similar to the standard stars PSFs resulting in an improved photometric accuracy.

Nod sets were shifted and registered before co-adding where necessary to avoid compromising photometric accuracy. Fig. 3.6 a) shows the coadded LWS image of the asteroid 2002 CT<sub>46</sub> observed on Feb. 21, 2003 without registering. Fig. 3.6 b) shows the same dataset after appropriate registering of each nod-set. The improvement in the S/N is clearly evident. Moreover, the shape of PSF of the resulting co-added registered image is more similar to the PSFs of the calibration standard stars, yielding to higher photometric accuracy of the derived final flux.

As in the case of Fig. 3.6 a), several asteroids were already visible in the original un-coadded frames. However, for the faintest ones, as in the case of 15817 Lucianotesi, 2000 EV<sub>70</sub> and 2001 HW<sub>15</sub> observed at Keck, the smearing effect was so strong to apparently compromise detection.

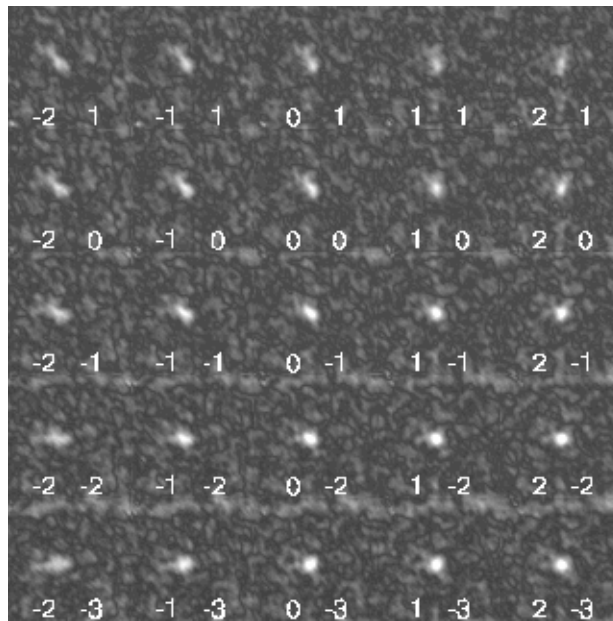


Fig. 3.7 The modulus of the cross correlation function between the instrumental PSF and frames registered with arbitrary shifts of the nod sets. Shown here is a 5×5 array of trials. The  $v_x$  and  $v_y$  values (see text) are indicated by the numbers at the bottom of each framelet.

A method for optimum registering of the nod sets was used in those cases. We have assumed that the largest contribution to the smearing effect was due to the non accurate tracking of the telescopes. In this hypothesis, the motion of the source from two successive nod-sets can be described by a vector  $(v_x, v_y)$ , where  $v_x$ , and  $v_y$  are the velocities of the source along the rows and the columns of the detector array. Under this assumption, the introduction of a shift to the  $i^{\text{th}}$  nod set of a quantity  $-(v_x, v_y) \times (t_i - t_0)$ , where  $t_i$  is the epoch at which the  $i^{\text{th}}$  nod-set was acquired, before coadding, allows the source to be properly registered. However, since the source is not visible on the unregistered frame,  $v_x$  and  $v_y$  are not known *a priori*. We have, therefore, registered nod sets with all possible combinations of velocities and

identified the optimal one with a cross-correlation of the registered image with the instrumental PSF obtained from the observation of a standard star. The best estimate for  $v_x$  and  $v_y$  is that set producing the registered frame with the highest value of the modulus of the cross correlation.

Fig. 3.7 shows a  $5 \times 5$  array of the modulus of the cross correlation function between registered frames of the asteroid 2000 EV<sub>70</sub> and the instrumental PSF, derived from the observation of the standard star  $\mu$ -UMa at 11.7  $\mu\text{m}$  with LSW at Keck1. It is clearly visible that by registering nod sets with  $v_x=1$  and  $v_y=-2$  (the fourth framelet from the left and from the top) and it is possible to obtain the final frame with the highest cross correlation.

### 3.8 Color correction

If  $T(\lambda)$  is the filter transmission function, the filter central wavelength may be defined by the following equation:

$$\lambda_c = \frac{\int_{-\infty}^{+\infty} T(\lambda) \lambda d\lambda}{\int_{-\infty}^{+\infty} T(\lambda) d\lambda} \quad (3-12)$$

The in-band flux of an astronomical source whose spectral energy distribution (SED) is described by the function  $F(\lambda)$  is given by the following equation:

$$F(\lambda_c) = \frac{\int_{-\infty}^{+\infty} T(\lambda) F(\lambda) d\lambda}{\int_{-\infty}^{+\infty} T(\lambda) d\lambda} \quad (3-13)$$

Let us suppose an observation yielded  $S''_{s \text{ tan dard}}$  counts and  $S''_{t \text{ arg et}}$  counts in the unit time. We can write that:

$$\int_{-\infty}^{+\infty} T(\lambda) F_{s \text{ tan dard}}(\lambda) d\lambda \frac{S''_{t \text{ arg et}}}{S''_{s \text{ tan dard}}} = \int_{-\infty}^{+\infty} T(\lambda) F_{t \text{ arg et}}(\lambda) d\lambda \quad (3-14)$$

where  $F_{s \text{ tan dard}}(\lambda)$  and  $F_{t \text{ arg et}}(\lambda)$  are the SED of the standard star and the unknown SED of the target asteroid respectively.

Assuming  $F_{t \text{ arg et}}(\lambda) = F_{t \text{ arg et}}(\lambda_c)$  to be constant within the filter bandwidth, Eq (3-14) may be simplified to

$$F_{target}(\lambda_c) = \frac{S''_{target}}{S''_{standard}} \times \int_{-\infty}^{+\infty} T(\lambda) F_{standard}(\lambda) d\lambda \bigg/ \int_{-\infty}^{+\infty} T(\lambda) d\lambda \quad (3-15)$$

where the second factor on the right-hand side of Eq (3-15) is the in-band flux of the standard star. However, the SED of the asteroid is not constant within the filter bandwidth and the use of Eq (3-15) yields to an error which has to be taken into account.

Without a loss of generality, we can assume the SED of the target to be described by a black-body at a given temperature multiplied by a scaling factor: i.e.  $F_{target}(\lambda) = \Omega B(\lambda, T)$ . The true value of the flux is therefore  $\Omega B(\lambda_c, T)$  which can be written in terms of  $F_{target}(\lambda_c)$  multiplied by a factor called color correction i.e.

$$\Omega B(\lambda_c, T) = F_{target}(\lambda_c) \times C_c \quad (3-16)$$

By equating the two in-band fluxes:

$$F_{target}(\lambda_c) \int_{-\infty}^{+\infty} T(\lambda) d\lambda = \Omega \int_{-\infty}^{+\infty} T(\lambda) B(\lambda, T) d\lambda \quad (3-17)$$

we can solve for  $\Omega$ . Once  $\Omega$  is inserted back into Eq (3-16), a solution for  $C_c$  can be found. This solution does not depend on  $F_{target}(\lambda_c)$  and is a function of the black-body temperature and the filter transmission curve only:

$$C_c = B(\lambda_c, T) \int_{-\infty}^{+\infty} T(\lambda) d\lambda \bigg/ \int_{-\infty}^{+\infty} T(\lambda) B(\lambda, T) d\lambda \quad (3-18)$$

Given the transmission profiles of the filters we have used at the LWS, TIMMI2, MIRLIN and MIRSI, Eq (3-18) can be used to calculate color correction factor for each filter as a function of the color temperature of the observed asteroids. Such color corrections are given in Appendix B.

### 3.9 Thermal IR spectroscopy at the TIMMI2

An N-band spectrum of the NEA 5587 was obtained at the ESO 3.6m telescope with the TIMMI2 on April 9, 2001. Since the target asteroid was bright enough, the differential tracking of the telescope was turned off and the autoguider was used to accurately track the proper motion of the small body keeping the source within the 3-arcsec-wide slit of the spectrograph. The low resolution grism was used to disperse the 7-13  $\mu\text{m}$  spectrum on the detector array (see Fig. 3.8).

The standard star HD123139 was observed at within 0.2 airmasses of the NEA 5587. The beam-switching observing mode was used (see Fig. 3.3). The field was chopped with a 10'' amplitude along the spectrograph slit. Nodding was performed by moving the telescope the opposite direction resulting in final co-added images where two positive spectra were superimposed approximately at the central row of the detector array and two negative spectra above and below the central channel (see Fig. 3.8). The data reduction has been carried out using IDL.

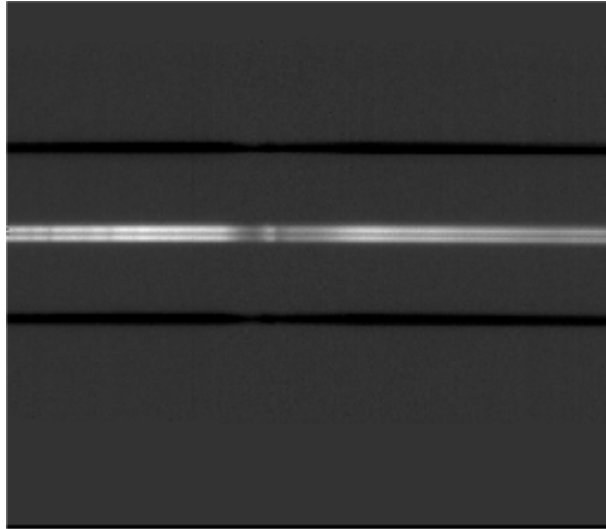


Fig. 3.8 Raw image of the N-band spectrum of the standard star HD123139 observed with the ESO 3.6m telescope and TIMMI2

The two negative spectra and the positive one were extracted separately and finally co-added. For each column, extraction of the raw spectra was accomplished by summing up the pixel values within a linear aperture 6 pixel wide centered on the signal and dividing the sum by the number of pixel of the aperture. The background value, to be subtracted on column basis, was defined as the median value of the pixels contained in two windows above and below the spectrum. Amplitudes and positions of the signal and background windows were defined by looking the one-dimensional spectral profile obtained by summing up the pixel values along each row of the infrared frames (see Fig. 3.9) i.e.

$$S''_{profile}(y) = \sum_x C''(x, y). \quad (3-19)$$

The signal-to-noise ratio of the raw spectra was derived assuming the background limited regime i.e. by using Eq (3-9).

Wavelength calibration in the N-band was performed by matching the atmospheric ozone absorption feature at about 9.5  $\mu\text{m}$  on the spectrum of the bright standard HD123139. The calibration

function was found to be well represented by a linear expression i.e.  $\lambda = 0.0114x + 8.0709$  where  $\lambda$  is the wavelength in  $\mu\text{m}$  and  $x$  the column coordinate on the detector array.

The absolute calibrated medium infrared spectrum of the target asteroid was obtained by taking the ratio of the raw spectrum of the target divided by the raw spectrum of the standard star multiplied by the spectral energy distribution (SED) of the latter. Of course resampling of the SED template of the standard star on those wavelengths corresponding to the detector columns was necessary.

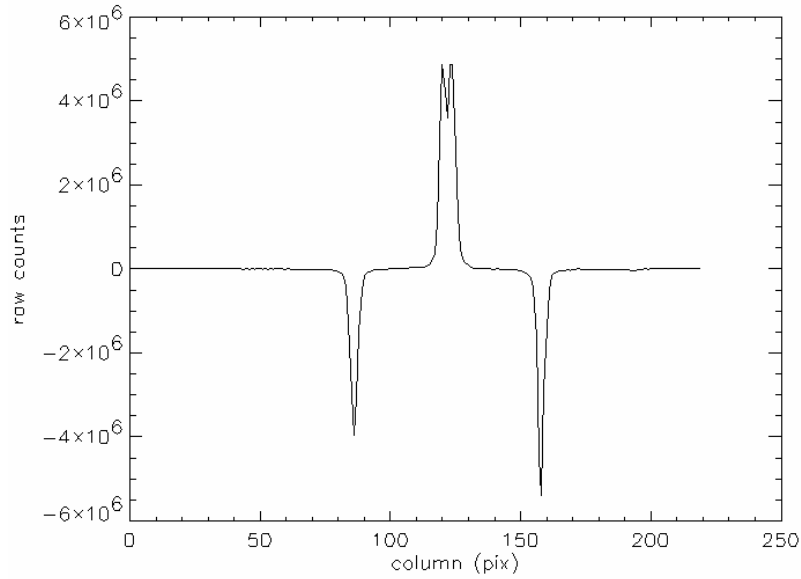


Fig. 3.9 The one-dimensional profile of the spectrum  $S''_{profile}(x)$ . It was obtained by summing up the contribution of all pixels along each row.

However, the low original S/N of the spectrum of the NEA 5587 would have produced poor quality results, if the raw spectra were not binned before the absolute calibration performed. A binning mask was therefore constructed and spectral regions of low signal to noise ratio (e.g. the ozone absorption feature at  $9.5 \mu\text{m}$ ) cutted off. The signal at each bin was computed by taking the mean of the raw values of the spectrum within each bin weighted by their signal-to-noise ratio. The wavelength of the center of the bin was used as the reference wavelength for the final data set. The final derived fluxes of the NEA 5587 and their uncertainties are listed in appendix A.

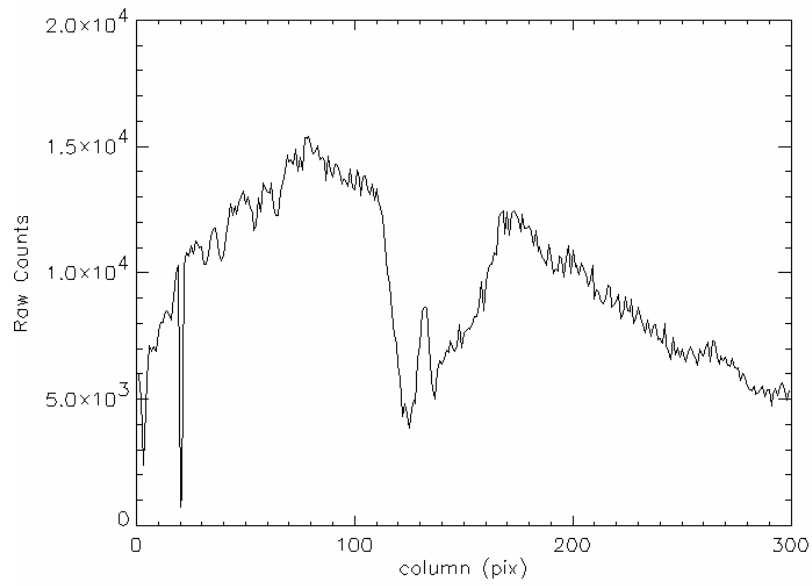


Fig. 3.10 Raw extracted spectrum of the standard star HD123139. Note the characteristic ozone feature between pixels 110-190

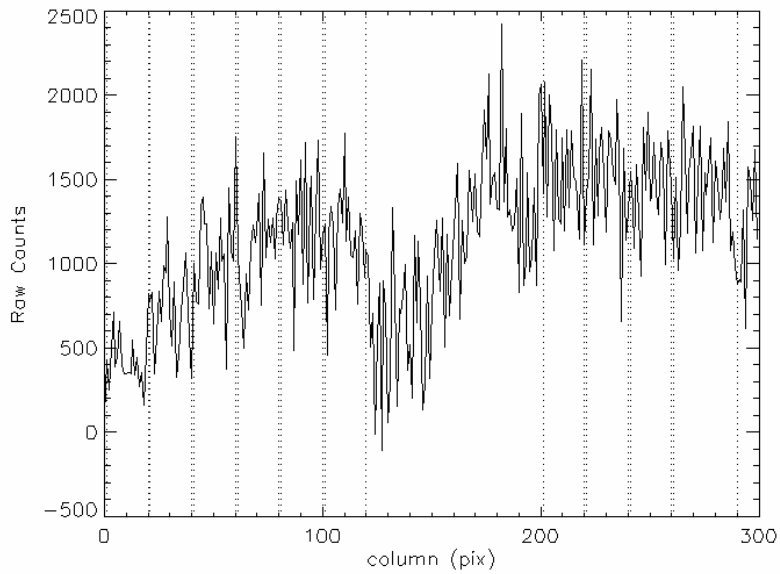


Fig. 3.11 N-band raw spectrum of the NEA 5587. Dotted vertical lines are drawn in correspondence to the bin extremes. The binning intervals were taken at the following detector columns (1 20), (21 40), (41 60), (61 80), (81 100), (101 120), (201 220), (221 240), (241 260), (261 290).

### 3.10 Visible CCD observations at ESO: data reduction

Visible CCD observations in the Johnson V filter, obtained with the DFOSC at the Danish 1.5 m telescope and with the WFI at the ESO/MPI 2.2 m telescope, were calibrated using the standard CCD data reduction scheme.

The digital to analog (D/A) converter of the CCD, introduces an offset to avoid negative digital numbers. In order to quantify and remove this offset from single CCD exposures a number of bias frames were obtained during the night. If the bias level was found to be constant or nearly constant during the night, an average bias frame (the so-called master bias) was calculated taking the median value of the biases for each pixel.

CCDs are affected by a pixel to pixel variation of the sensitivity. To obtain a map of the sensitivity, flat-field images are obtained for each set up used during the observation. A flat-field frame is obtained by imaging a homogeneously illuminated surface such as a screen in the dome or the sky at dusk or at dawn. A master flat is calculated by taking the median value for each pixel from a series of normalized flat fields.

Each raw CCD exposure  $R(x,y)$  was calibrated using Eq. 3-21

$$I(x, y) = \frac{R(x, y) - B(x, y)}{F(x, y) - B(x, y)} \times K \quad (3-20)$$

where  $I(x,y)$  is the final image,  $B(x,y)$  is the master bias,  $F(x,y)$  the master flat and  $K$  is a multiplicative factor equal to the mean level of the master flat.

Using the ATV package, aperture photometry was performed on each CCD image to derive raw counts for the target asteroids and a number of reference stars. The basic formula to calculate the differential magnitude between object  $i$  and  $j$  is then  $\Delta m_{ij} = -2.5 \log_{10}(f_i / f_j)$ , where the  $f$  values are the number of raw counts measured for each source.

Usually, when doing differential CCD photometry, it is common to consider the field covered by the CCD to be small compared to the variations in extinction over the sky. The airmass is thus the same for the asteroid of interest and the reference stars contained within the same CCD image. In the case of fast-moving objects such as NEOs close to the Earth it is not, in general, possible to use the same reference stars throughout the whole night. Formally we get a set of short lightcurves, one for each reference star. The intuitive way to connect the set into a long lightcurve might be to calculate the differential magnitude between the reference stars in those frames where they overlap. The short curves

would then have to be shifted up or down in order to compensate for the magnitude differences among the reference stars.

We have used the method of Erikson et al. (2000) to properly connect the short light curves. This procedure is to first fit the stars into a magnitude system by a least-square method and then use this system to derive the full lightcurve of the asteroids.

By plotting the instrumental magnitudes of the comparison stars as function of the airmass, we have derived the atmospheric extinction coefficients. Observation of standard stars (Landolt's fields) throughout the night yielded absolute calibration of the magnitude scale and the derivation of  $V(r, \Delta, \alpha)$  apparent magnitude of the target asteroids at the heliocentric distance  $r$ , geocentric distance  $\Delta$  and phase angle  $\alpha$ . Given  $V(r, \Delta, \alpha)$  at lightcurve mean for each asteroid, the absolute magnitudes  $H \equiv V(r=1, \Delta=1, \alpha=0^\circ)$ , i.e. the magnitude that an asteroid would have at 1AU from the Sun and the Earth and at zero degree of phase angle, were calculated using the standard method described by Bowell et al. (1989), appendix A.

### 3.11 The data set

Table 3-1, lists relevant observational circumstances and physical data for the target asteroids observed at Keck. Note that Table 3-1 contains three more NEAs, with respect to the equivalent table of Delbò et al. (2003). These three objects, 15817 Lucianotesi, 2000 EV<sub>70</sub> and 2001 HW<sub>15</sub>, were extremely faint. Telescope tracking inaccuracy smeared their weak signal on the final co-added image compromising detection. Only the use of a new method, described in Appendix B, allowed blind registering of the nod-sets and yields their detection in the thermal infrared images obtained at LWS.

Table 3-2 shows equivalent information for the asteroids observed at ESO and Table 3-3 for the observations carried out at the NASA-IRTF. The resulting fluxes are listed in appendix A.

The quoted uncertainties in the flux measurements refer to the statistical uncertainties in the synthetic aperture photometry procedure only. Errors in the absolute calibration and fluctuations in atmospheric conditions during the observations increase the scatter in the flux data.

### 3.11.1 Near-Earth asteroids observed at KECK

Object	H (mag)	Date	$\alpha^\circ$	R (AU)	$\Delta$ (AU)	Lightcurve		Notes
						Per. (h)	amp. (mag)	
1627 Ivar	12.87±0.1	00-03-16	5	2.057	1.073	4.795	0.35	a
1866 Sisyphus	13.00	00-03-17	16	2.903	2.194	2.400	0.11	b
2100 Ra-Shalom	16.11±0.1	00-08-21	39	1.175	0.222	19.79	0.40	a, f
4034 1986 PA	18.2	01-05-11	40	1.219	0.299	-	-	
4055 Magellan	14.90±0.1	00-03-16	13	2.058	1.122	7.475	0.46	a
4660 Nereus	18.7	02-02-21	60	1.033	0.093	15.1	0.6	
5587 1990 SB	14.1±0.5	01-05-10	42	1.213	0.301	5.052	1.1	a
5604 1992 FE	17.72±0.1	01-05-11	36	1.301	0.392	-	-	c
5751 Zao	14.93±0.07	01-05-12	49	1.250	1.180	21.7	0.12	d
14402 1991 DB	18.85±0.1	00-03-16	36	1.076	0.103	2.266	~0.1	a
15817 Lucianotesi	18.6	00-03-17	14	1.275	0.291	11.0	0.8	
16834 1997 WU <sub>22</sub>	15.9±0.5	00-08-21	59	1.142	0.331	9.348	0.4	a, f
19356 1997 GH <sub>3</sub>	17.0	01-05-11	5	1.421	0.413	6.714	0.74	
25330 1999 KV <sub>4</sub>	16.3	01-05-10	54	1.201	0.425	-	~0.1	
1999 FK <sub>21</sub>	18.0	02-02-21	35	1.142	0.195	-	-	
1999 NC <sub>43</sub>	16.1±0.5	00-03-17	59	1.130	0.366	34.5/122.3?	1.1	a
2000 BG <sub>19</sub>	17.8	00-03-17	17	1.396	0.429	-	-	
2000 EV <sub>70</sub>	20.3	00-03-17	14	1.119	0.128			
2000 PG <sub>3</sub>	15.74	00-08-21	2	2.118	1.108	-	≤ 0.2	f
2001 FY	18.8	01-05-12	22	1.269	0.285	-	-	
2001 HW <sub>15</sub>	20.2	01-05-12	11	1.152	0.145	-	-	
2002 BM <sub>26</sub>	20.1	02-02-21	60	1.024	0.074	~ 2.7	-	e
2002 CT <sub>46</sub>	20.8	02-02-21	23	1.107	0.129	-	-	

Table 3-1 Observational circumstances and relevant data for the Keck targets. Where no other source is given, H-values are from the web services given in section 2.8.3.

- a. Lightcurve data and mean H derived from photometry made during the apparition of the Keck thermal observations by Pravec and colleagues. In the cases of (5587), (16834), and 1999 NC43 only rough H-values could be estimated due to the high phase angle of the observations.
- b. Lightcurve data from A.W. Harris. ([cfa-www.harvard.edu/iau/lists/LightcurveDat.html](http://cfa-www.harvard.edu/iau/lists/LightcurveDat.html)).
- c. H-value and lightcurve data from from observations carried out at ESO, La Silla (see section 4.3.11)
- d. Lightcurve data and mean H taken from Pravec et al. (1997). The H-value should also be valid for the 2001 apparition to an accuracy of ~ 0.1 mag as the asteroid showed little aspect-related variation in earlier apparitions.
- e. Rotational period of ~ 2.7 h from Nolan et al. (2002).
- f. Observations were carried out under poor observing conditions

### 3.11.2 Near-Earth asteroids observed at ESO

Object	H (mag)	Date yymmdd	$\alpha^\circ$	R (AU)	$\Delta$ (AU)	Lightcurve		Notes
						Per. (h)	amp. (mag)	
5381 Sekmeth	16.5	03-06-02	44	1.176	0.247	0.35	~0.35	g
2001 LF	17.4	03-06-02	45	1.173	0.244			h
		03-06-03	45	1.173	0.244			
2002 AV <sub>4</sub>	15.8	03-06-01	70	1.071	0.266			
37314 (2001 QP)	14.6	01-12-04	38	1.416	0.568			
12008		01-04-09	36	1.033	1.639			
33342(1998 WT <sub>24</sub> )	18.54±0.1	01-12-04	60	1.015	0.062	3.72336	~0.2	i
5587 1990 SB	14.1±0.5	01-04-08	20	1.412	0.448	5.052	1.1	k
		01-04-09	19	1.405	0.439			j, k
5604 1992 FE	17.72±0.1	01-05-11	36	1.301	0.392	-	-	c
25143 Itokawa	19.48	01-04-08	108	0.983	0.054			l
		01-04-09	110	0.981	0.056			
35396 (1997 XF <sub>11</sub> )	17.1±0.1	02-11-28	30	1.218	0.279	3.25	~0.7	
2002 QE <sub>15</sub>	16.3	02-11-28	50	1.132	0.261			
19356 1997 GH <sub>3</sub>	17.0	01-04-08	32	1.209	0.256	6.714	0.74	k
		01-04-09	31	1.215	0.259			
25330 (1999 KV <sub>4</sub> )	16.3	03-06-02	16	1.497	0.513	4.919	0.15	k

Table 3-2 Observational circumstances and relevant data for the targets observed at ESO. Where no other source is given, H-values are from the web services given in section 2.8.3.

- g. Lightcurve data from ESO but H-values are from the web services give in section 2.8.3
- h. H-value from Dandy et al. (2003)
- i. H-value, derived assuming  $G=0.40$  (E type), and lightcurve data from from observations carried out at ESO, La Silla (see section 04.3.13)
- j. Data obtained from thermal infrared spectroscopy in the N and Q band.
- k. Lightcurve data and mean H derived from photometry made during the apparition of the ESO thermal observations by Pravec and colleagues.
- l. H value from Abe et al., 2002.

### 3.11.3 Near-Earth asteroids observed at the NASA-IRTF

Object	H (mag)	Date yymmdd	$\alpha^\circ$	R (AU)	$\Delta$ (AU)	Lightcurve		Notes
						Per. (h)	amp. (mag)	
33342(1998 WT <sub>24</sub> )	18.54±0.1 E	01-12-18	67	0.990	0.016			m
		01-12-19	79	0.987	0.020			m
		01-12-21	93	0.982	0.028			m
1580 Betulia	14.0	02-06-02	53	1.143	0.246			
25330 (1997 KV <sub>4</sub> )	16.3	03-05-14	03	1.396	0.386	-	~0.1	
5381 Sekmeth	16.5	03-05-12	42	1.114	0.146	0.35	~0.35	n
		03-05-13	38	1.117	0.140			n
		03-05-14	33	1.121	0.135			n
		03-05-15	29	1.124	0.132			n
		03-05-16	24	1.128	0.129			n,o
6489 Golevka	19.07±0.03	03-05-15	43	1.081	0.099			p
35396 (1997 XF <sub>11</sub> )	17.1±0.1 E	02-11-03	63	1.022	0.070	3.25	~1.0	q
	17.1±0.1 E	02-11-05	53	1.038	0.080	3.25	~1.0	q

Table 3-3 Observational circumstances and relevant data for the targets observed at the NASA-IRTF. Where no other source is given, H-values are from the web services given in section 2.8.3. Observations of the NEA 35396 (1997 XF<sub>11</sub>) were carried out with MIRS. All other objects have been observed using MIRLIN

- m. H-value, derived assuming  $G=0.40$  (E type), and lightcurve data from from observations carried out at ESO, La Silla (see section 04.3.13)
- n. Lightcurve data from ESO but H-values are from the web services give in section 2.8.3
- o. Presence of cirrus was noted
- p. H value from Mottola et al. (1997)
- q. H-value and lightcurve data from from observations carried out at ESO, La Silla (see section 4.3.14)

### 3.12 Summary

Thermal infrared observations (5-20  $\mu\text{m}$ ) were collected primarily using the LWS installed at the Keck 1 telescope, Mauna Kea, Hawaii. A related project, started in April 2001, was awarded 10 nights at the ESO, La Silla (Chile). The TIMMI2 at the 3.6 m telescope was used to perform thermal infrared observations while the 1.5 m Danish and the 2.2 m ESO/MPI telescopes were used to obtain simultaneous V magnitudes. The NASA-IRTF has also been used with the aim of performing detailed study of selected targets.

Overall, 32 asteroids were observed. For 7 of them observations were collected under different geometries and with different instruments. Fig. 3.12 shows histograms of the number of observations as a function of the absolute magnitude, H, of the target asteroids and the as a function of the solar phase angle. From these plots it is evident that our program gathered radiometric observations mainly of the sub-kilometer population of Earth crossing asteroids. Furthermore, the large range of solar phase angles spanned by our observation allows detailed study of the thermal properties of the targets and a refinement of the thermal models to be performed.

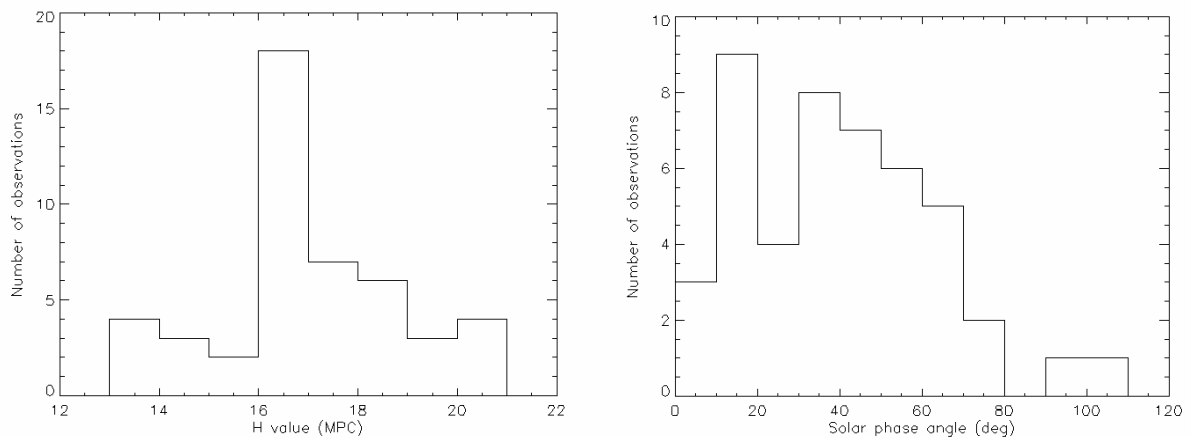


Fig. 3.12 Histogram of the number of observations as a function of the absolute magnitude H of the target asteroids and the as a function of the solar phase angle. H values for each object are obtained from the MPC. 7 objects out of 32 were observed with different instrument and under different observing geometries.

Thermal infrared ground based observations are limited to the M ( $\sim 5 \mu\text{m}$ ), the N (between  $\sim 8$  and  $13 \mu\text{m}$ ) and the Q ( $\sim$  between  $17.5$  and  $22 \mu\text{m}$ ). On the basis of the experience gained during this work typical measurements accuracy are of the order of 10-15% in the M and Q band and about 5% in the N

band. For 17 targets, which were found to be very weak, observations were obtained with N-band filters only.

To subtract the strong contribution of the background, observations were carried out using the chopping-nodding technique.

Differential tracking was used to minimize the effect of the large proper motion of the target asteroids. Nevertheless, in some cases registering nod-sets before coadding was necessary to avoid smearing effects.

A new method, discussed in section 3.7, have been used to search for and identify in apparently void LWS images three more asteroids observed at Keck.

Aperture photometry was performed to calculate the signal of the infrared sources. Cohen et al. (1999) standard stars were used for absolute flux calibration and they were imaged within 0.1 – 0.2 airmasses of the targets asteroids.

Color corrections were evaluated and found to be only a few percent for the filters used to carry out our multi-wavelengths observations. Color corrections were thus not applied to correct the final monochromatic flux densities derived and listed in Appendix A.